Original

Lazaneo, C.; Calil, P.; Tandon, A.; da Silveira, I.:
Submesoscale Coherent Vortices in the South Atlantic Ocean: A Pathway for Energy Dissipation.
In: Journal of Geophysical Research : Oceans. Vol. 127 (2022) 2, e2020JC017099.

First published online by AGU: 20.01.2022

https://dx.doi.org/10.1029/2020JC017099

JGR Oceans

RESEARCH ARTICLE
10.1029/2020JC017099

Submesoscale Coherent Vortices in the South Atlantic Ocean: A Pathway for Energy Dissipation

C. Z. Lazaneo[1,2], P. H. R. Calil[3], A. Tandon[2], and I. C. A. da Silveira[1]

[1]Instituto Oceanográfico, Universidade de São Paulo, São Paulo, Brazil, [2]School for Marine Science and Technology, University of Massachusetts Dartmouth, Dartmouth, MA, USA, [3]Institute of Carbon Cycles, Helmholtz-Zentrum Hereon, Geesthacht, Germany

Key Points:

- Submesoscale coherent vortices (SCV) are observed around the complex topography of the Vitória-Trindade Ridge
- Small-scale turbulence inside the SCVs can cascade energy down to dissipation via centrifugal and symmetric instabilities
- The amount of turbulent kinetic energy dissipation within the SCV is comparable to that of the mixed layer

Supporting Information:

Supporting Information may be found in the online version of this article.

Correspondence to:

C. Z. Lazaneo,
cauezlazaneo@usp.br

Citation:

Lazaneo, C. Z., Calil, P. H. R., Tandon, A., & da Silveira, I. C. A. (2022). Submesoscale coherent vortices in the South Atlantic Ocean: A pathway for energy dissipation. *Journal of Geophysical Research: Oceans*, *127*, e2020JC017099. https://doi.org/10.1029/2020JC017099

Received 17 DEC 2020
Accepted 12 JAN 2022

Abstract Mesoscale eddies propagate westward across the South Atlantic basin. As they reach the westernmost part of the basin, at approximately 20°S, they interact with a quasi-zonal seamount chain, the Vitória-Trindade Ridge (VTR). The interactions with the local topography lead to submesoscales instabilities, which ignite the formation of submesoscale coherent vortices (SCVs) such as those described in the present study for the first time in the VTR region. Here, using high-resolution hydrographic and microstructure measurements, we describe the dynamics of two adjacent SCVs wandering through the ridge. We find that the anticyclonic SCVs are characterized by a low potential vorticity and angular momentum signature, and are therefore prone to both centrifugal and symmetric instabilities. This dynamic regime suggests small-scale turbulence is actively cascading energy down to dissipation, diagnosed from turbulent kinetic energy dissipation estimates within one of the SCVs through microstructure measurements. The energy dissipation levels observed within the SCV are two orders of magnitude larger than in surrounding waters. The thermohaline signatures of each SCV reveal homogenized waters in their cores but with small thermohaline anomalies when compared to surrounding waters, suggesting a remote generation site. Here, we argue that such vortices are essential agents for energy dissipation in the ocean. We speculate that the observed SCVs were formed due to mesoscale eddy-topography interaction along the VTR and advected by the meandering South Equatorial Current to the location of field observations.

Plain Language Summary The interaction between topography and oceanic flows results in the development of small-scale turbulent phenomena. The occurrence of such phenomena is significant for the ocean energy balance due to energy dissipation, which occurs on spatial scales smaller than a centimeter. In this study, we describe, for the first time in the western South Atlantic Ocean, the physics of two adjacent submesoscale coherent vortices in the vicinity of the Vitória-Trindade Ridge. These vortices have radii of 12 and 16 km and a subsurface signature with intensified velocity and weak stratification. Since this type of vortex has no surface expression, it is challenging to detect it due to its small horizontal scale. Microstructure measurements collected by a ship inside and outside the vortex enable us to evaluate, for the first time, its influence on energy dissipation and ocean mixing.

1. Introduction

The majority of the ocean's kinetic energy remains at mostly balanced mesoscale and large-scale flows. While geostrophically balanced eddies transfer energy to larger scales via an inverse cascade (Charney, 1971), different mechanisms can remove energy from geostrophic flows and transfer it to unbalanced motions at smaller scales. This forward cascade is modulated by submesoscale motions that act as a transition from the mostly two-dimensional, geostrophically balanced dynamics to the full three-dimensional flows where dissipation occurs (McWilliams, 2016; Thomas et al., 2008).

Flow-topography interactions disturb the geostrophic balance and may lead to submesoscale instabilities. The incoming flow against the sloping topography increases bottom drag which leads to intense vertical vorticity influx into the flow. Observations reveal the formation of vortices due to flow-topography interaction in most of the world's oceans (D'Asaro, 1988; Gula et al., 2016, 2019; Molemaker et al., 2015; Srinivasan et al., 2017, 2019; Vic et al., 2015). The vorticity filaments merge into the topographic wake to eventually form submesoscale coherent vortices (SCVs; McWilliams, 1985).

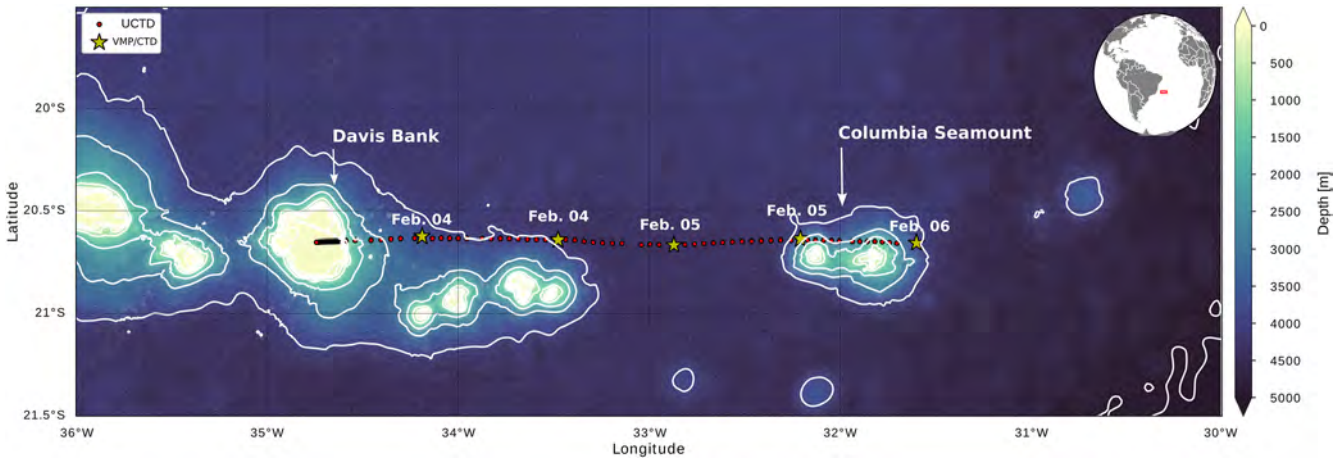

Figure 1. Part of the Ilhas 1 austral summer survey, 3–6 February (transect 6–T6). Map of the Vitória-Trindade Ridge region, with the light yellow shading representing depths shallower than 300 m. Red dots and yellow stars indicate the locations of Underway Temperature, Conductivity, and Depth and Vertical Microstructure Profiler/CTD stations, respectively. The thick white lines represent the 4,000, 3,000, 2000, 1,000, 500, 250, 100, and 50 m isobaths. Long-time-averaged shipboard-Acoustic Doppler Current Profiler velocities were measured along the transect beginning at the Davis Bank in the west, and ending at the Columbia Seamount.

Such vortices, also called intrathermocline eddies (Dugan et al., 1982), are often described as swirl-like currents and are predominantly associated with distinct, convex-lens-shaped tracer anomalies (Frenger et al., 2018; Gula et al., 2019). The convex-lens-shaped anomalies are only for anticyclonic SCVs. Though less abundant, SCVs can also be cyclonic (e.g., de Marez et al., 2020). The SCVs are characterized by radii smaller than the Rossby baroclinic deformation radius, with Rossby (*Ro*) and Burger (*Bu*) numbers of $\mathcal{O}(1)$ (McWilliams, 1985). Once formed, SCVs can wander in the interior of the ocean for many years (McWilliams, 2016), thus acting as important agents of long-range tracer transport since they retain waters from their formation sites as they propagate as coherent structures.

SCVs are present in all of the world's oceans (McCoy et al., 2020). Meddies, for example, are SCVs that flow from the Mediterranean Ocean, transporting a great amount of salt into the Atlantic Ocean (McDowell & Rossby, 1978). Puddies, which are SCVs typically formed in the eastern boundary poleward undercurrents, tend to maintain their coherence for hundreds of kilometers while propagating westward and feeding the subtropical gyres with nutrient-rich waters (Frenger et al., 2018). SCVs are also formed due to the interaction of boundary currents with topography as in the Beaufort Gyre (D'Asaro, 1988), the Charleston Bump and Cape Hatteras (Bane et al., 1989; Gula et al., 2019), and the Mid-Atlantic Ridge (Vic et al., 2018). Despite the ubiquity of SCVs, their generation mechanisms, as well as their role in the general ocean circulation, are still not fully known.

Most SCVs do not have a surface expression, and it is challenging to detect them due to their small horizontal scale (Assassi et al., 2016). They have been observed in moorings (Bane et al., 1989), hydrographic profiles from ships (Dugan et al., 1982), and more recently by glider measurements and in seismic images of the ocean (Gula et al., 2019; Ménesguen et al., 2012). Thus, observations at high spatial resolution, able to capture more than a single profile inside one of these features are still challenging. The Vitória-Trindade Ridge (VTR) in the South Atlantic Ocean (Figure 1) may be a hotspot for SCV generation due to the presence of many shallow seamounts, banks, and islands (Alberoni et al., 2020) along the path of the Brazil Current, which is formed just a few degrees north of the VTR. In addition, westward propagating eddies usually interact with the VTR since this ridge is in the path of the flow of the South Equatorial Current (SEC).

We conducted a high-resolution oceanographic survey in the austral summer of 2017 in order to investigate the impact of the seamount chain on the flow field. In this work, we describe the structure of two anticyclonic SCVs observed near a shallow seamount, the Columbia Seamount, which is part of the VTR. We also present observations of the turbulent regime inside one of the features. To the best of our knowledge, this is the first time microstructure measurements of mixing were taken inside an SCV.

The article is organized as follows. In Section 2, we present the sampling strategy. In Section 3, we describe the vertical structure of two SCVs near the VTR. In Section 4, we present the first microstructure measurements within one SCV observed in the real ocean. In Section 5, we address one of the possible regions of origin of the observed SCVs. Summary and concluding remarks are presented in Section 6.

2. The Ilhas 1 Survey Data Set

During the austral summer of 2017, we conducted an oceanographic survey (Ilhas 1, from January 27 to February 16) aboard the *R/V Alpha-Crucis* (University of São Paulo) as part of the "Islands" experiment in the vicinity of the VTR. The main purpose of this survey was to elucidate the role of seamounts in the generation of submesoscale features due to the interaction of the rich mesoscale eddy field with the local topography.

The VTR is a quasi-zonal ridge that extends 1,120 km from the Abrolhos shelf to the Trindade and Martin-Vaz Islands (Figure 1). Except for these islands, the ridge is entirely submerged and composed of flat-top seamounts and banks, most of them with summits between 55 and 75 m below the surface (Alberoni et al., 2020). The eddy activity on the VTR makes it an ideal place to study mesoscale flow-topography interaction. Throughout the cruise, starting at the Davis Bank and ending at the Columbia Seamount (CS), we measured the velocity continually with a Vessel-Mounted Acoustic Doppler Current Profiler (VM-ADCP, *Teledyne RDI - 75* kHz) set to sample at 8m vertical bins. Data were processed using the CODAS (Common Ocean Data Access System) software, following the guidelines of Firing (1995). Simultaneously, hydrographic data were obtained using an Underway Temperature, Conductivity, and Depth (UCTD, *Teledyne Oceanscience*) probe at a high spatial resolution. Over the Davis Bank, the spatial resolution of temperature and salinity profiles was approximately 1 km. Over deep regions, the spatial resolution of profiles was around 5 km (30 min apart), but reaching deeper levels (approximately 450 m). We estimated the turbulent parameters from microscale shear variance measurements at five oceanographic stations (Figure 1). A Vertical Microstructure Profiler (VMP - 250 *Rockland Scientific*), operating at 512 Hz, was equipped with two shear probes, one SBE7 micro-conductivity probe and one FP07 thermistor. The VMP operated in downcast mode (free-falling profile), and for statistical reliability, we performed at least three casts at each station (e.g., Doubell et al., 2018; Lazaneo et al., 2020). The CTD (Seabird) profiles were carried out at the same oceanographic stations where the VMP profiles were carried out, collecting conductivity, temperature, and dissolved oxygen measurements. The mesoscale surface field was estimated using the altimeter measurements distributed by the Copernicus Marine and Environment Monitoring Service (CMEMS, http://marine.copernicus.eu).

3. The SCV Vertical Structure

During the Ilhas 1 survey, we observed a mesoscale anticyclone over the CS through the objective mapping (correlation lengths: $\Delta x = 30$ km and $\Delta z = 50$ m) of the horizontal velocity measured by the ADCP along the zonal section depicted in Figure 1. The measured surface velocity agrees with the surface geostrophic velocity field from the altimeter (Figure 2). The subsurface maximum velocity occurred in the anticyclonic meander, driving large anomalous values of relative vorticity, obtained, in this case, from the zonal gradient of the meridional velocity ($\zeta = \partial v/\partial x$). $\mathcal{O}(1)$ gradient Rossby numbers ($Ro = \zeta/f$, where f is the planetary vorticity) indicate the deviations from the dominant geostrophic balance (Figure 3). In addition to the intense Ro values at the location of the subsurface velocity maximum, the geostrophic velocity estimated from the density field (thermal-wind balance) presents lower magnitudes compared to the measured velocity (see Supporting Information S1). Qualitatively, the estimated velocity field is in agreement with the measured velocities. They differ only in magnitude. Once the velocity patterns are qualitatively in accordance but slightly different in magnitude, it suggests that the subsurface flow is not necessarily geostrophic. The presence of a flow with a non-negligible ageostrophic component and Ro of $\mathcal{O}(1)$ is indicative of a subsurface submesoscale phenomenon, which in this case, is bounded by double convex-lens-shaped isopycnals. Despite the spatial variability of the isopycnals (Figure 3), the configuration of the two convex lenses is maintained in the objective mapping of density (not shown, same correlation lengths used for velocities). This flow configuration indicates the existence of two interacting anticyclonic SCVs, which may have been generated by the interaction of the meandering flow of the SEC with the isolated topographic features east of the 32°W. The meandering flow of the SEC presents a trajectory passing through the topographic features of the VTR (Luko et al., 2021). Therefore it tends to generate intense relative vorticity in the subsurface

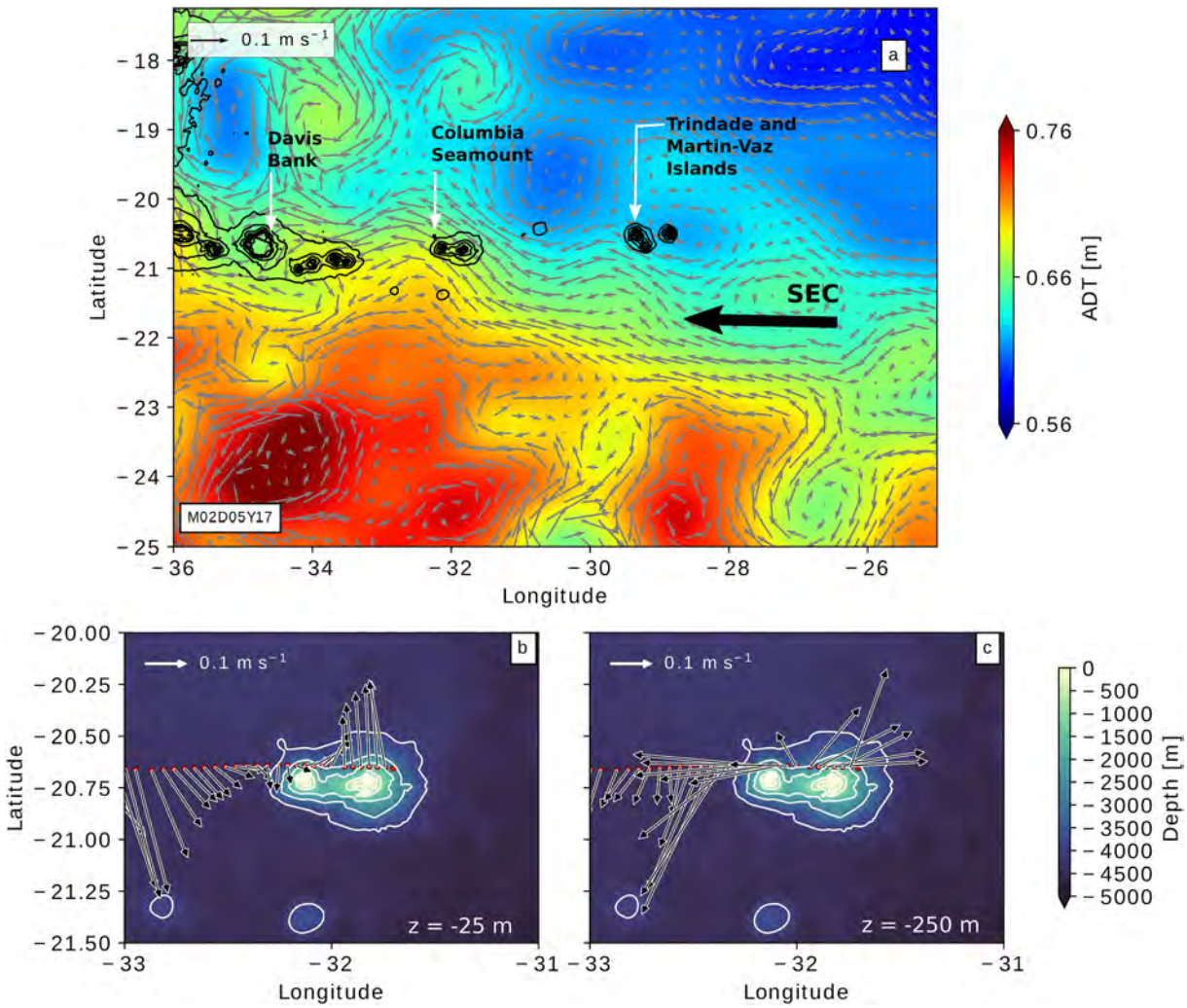

Figure 2. (a) Vitória-Trindade Ridge region map for 5 February 2017, with the background color representing absolute dynamic topography, and gray arrows indicating the geostrophic velocity. Bottom panels are the Columbia Seamount region map, with the light yellow shading representing depths shallower 300 m, and with the (b) surface and (c) subsurface velocities obtained by the Acoustic Doppler Current Profiler. The (a) black and (b and c) white lines represent the 4,000, 3,000, 2000, 1,000, 500, 250, 100, and 50 m isobaths.

due to frictional effects in the bottom boundary layer of the islands and seamounts of the ridge, which ultimately triggers the generation of SCVs. Inside one of these SCVs, we also observed anomalous dissolved oxygen values (Figure 3e), suggesting, in fact, the presence of a such subsurface vortex, which may have been generated remotely. Chemical property anomalies are characteristic of SCVs, which, due to their coherence, carry water from the region of origin (McWilliams, 1985).

To illustrate the eddy interaction, we present in Figure 4 a schematic diagram of two adjacent anticyclones (see Supporting Information Figure S2), as well as the associated vertical component of the relative vorticity and horizontal divergence. We notice alternating bands of anomalous values of both quantities (Figures 4b and 4c), such as those depicted in the fields of the observed SCVs (Figure 3). Indeed, our observations show these alternating bands of $(\partial v/\partial x)$ and $(\partial u/\partial x)$ bounded by the isopycnal inflections that delimit the vortical features. We therefore interpret this interaction of two vortices with the same rotation sense as a submesoscale version of the Fujiwhara effect in the ocean.

In order to identify the intersection region between the SCVs and their limits with the surrounding waters, next we characterize the temperature and salinity signatures along the transect. Temperature (Figure 5a) and salinity (Figure 5b) present a heterogeneous horizontal distribution, with the most consistent variations associated with

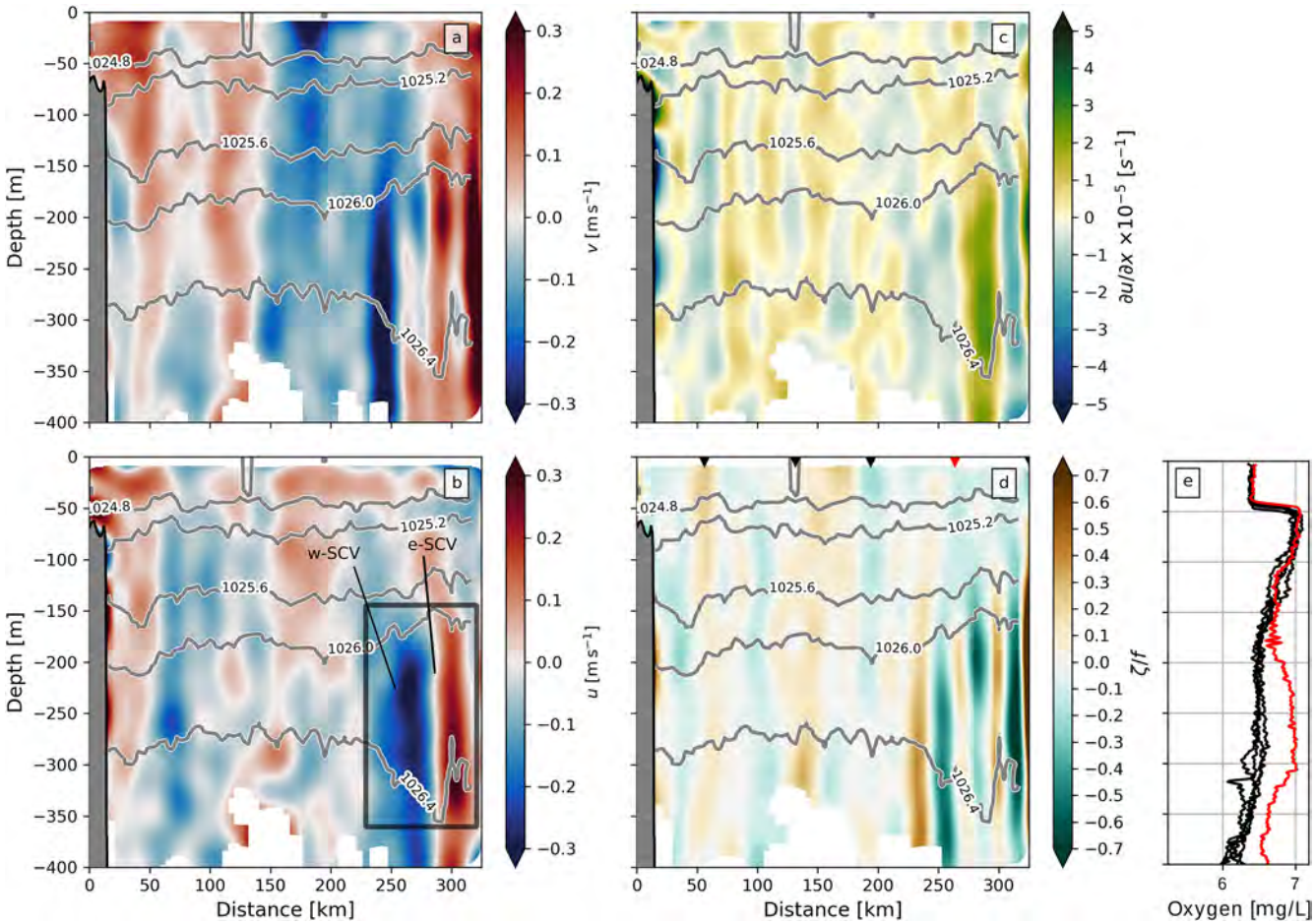

Figure 3. Vertical section of the (a) meridional velocity component, (b) zonal velocity component, (c) divergence considered as $\partial u/\partial x$, and (d) ζ/f. Gray contours represent the isopycnals [kg m^{-3}] along the section. The origin of the transect starts at the Davis Bank (~20.6°S, 34.7°W). The black rectangle encloses the location of the submesoscale coherent vortices (SCVs). (e) Vertical profiles of dissolved oxygen obtained from the CTD. The location of CTD station are depicted in panel (d). The red profile represents the station over the SCV.

the location of subsurface velocity maximum. However, the deepening of isopycnals at ~268 km from the origin of the transect – Davis Bank – demarcates the horizontal limit of the two adjacent SCVs. Despite the sharp inflections of the isopycnals in between the SCVs, weak stratification prevails within both convex lens-shaped isopycnals (Figure 5c). Further, both SCVs depict the same water mass content, which ultimately suggests that their generation sites may have been within the South Atlantic Central Water domain (SACW, see Stramma & England, 1999) (Figure 5d) but at levels close to the most stratified layer (Figure 5c), which presents the greatest oxygen content (Figure 3e). The anomalous patterns in the temperature and salinity zonal distributions along some selected depths (−200 m, −250 m, −300 m) within the two SCVs not only elucidate their boundaries relative to the surrounding waters but also can be indicative of density compensation and mixing processes (Figures 6b–6d). Aiming to verify the occurrence of density compensation at the SCV boundaries, we compute the spiciness variation ($\Delta\tau$) (Ferrari & Rudnick, 2000; Munk, 1981; Veronis, 1972)

$$\Delta\tau = (\alpha\Delta T) + (\gamma\Delta S), \tag{1}$$

where α is the thermal expansion coefficient, and γ is the saline contraction. Our results show that spicy waters (warm and salty) mark the contact region between the SCVs, while minty waters (fresh and colder) are found in both SCV cores (Figure 6a). These spiciness signatures are indicative of double-diffusion processes and mixing. The temperature and salinity profiles at the center of each SCV highlight the density compensation processes and mixing (Figures 6e–6g). The SCV core to the west (w-SCV) has colder and fresher waters compared to the vortex waters to the east (e-SCV). Noting the temperature and salinity of the profile outside the vortices between −200

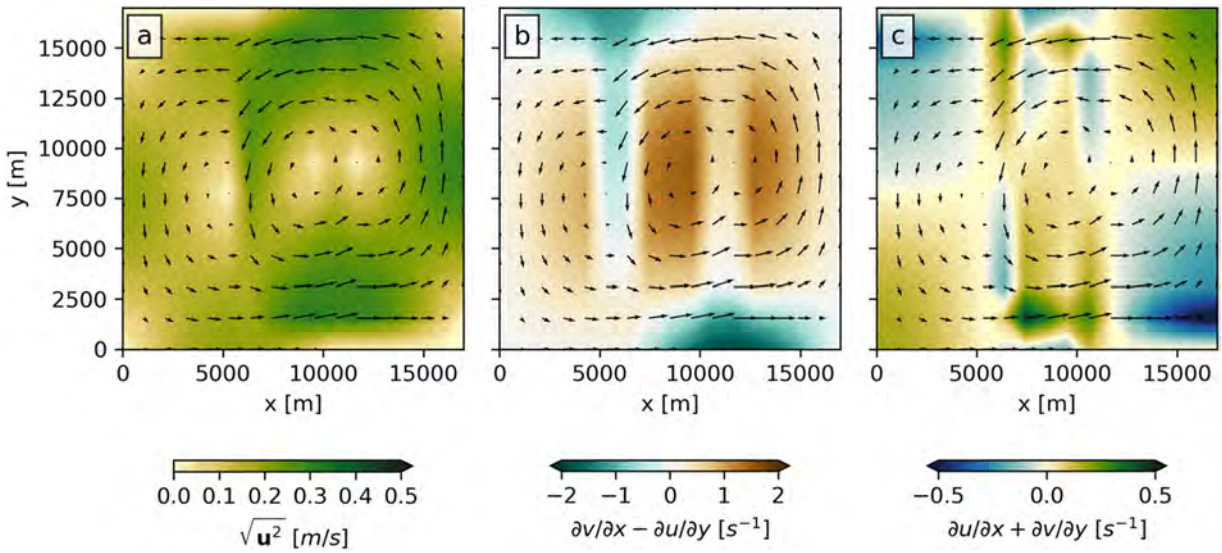

Figure 4. (a) Two-dimensional depiction of two adjacent anticyclones, as well as (b) the associated vertical component of the relative vorticity and (c) horizontal divergence. Black arrows are the velocity vectors from the velocity field.

and −350 m, we observe that these profile segments have thermohaline properties different from the SCV core waters (Figures 6e–6g). These signatures suggest that the SCVs were generated remotely but not necessarily far from the observation site (e.g., Gula et al., 2019; McWilliams, 1985).

Given the horizontal limits of the SCVs shown in Figure 6, the w-SCV has an $l = 12$ km radius, and the e-SCV has an $l = 16$ km radius, assuming that we crossed the SCVs through their center. These values correspond respectively to about 20% and 28% of the full-depth first baroclinic deformation radius $R_D \sim 56$ km, which was estimated from the climatology following Houry et al. (1987). By combining the length and depth scales obtained by the thermohaline data analysis with the velocity measurements, we estimate dimensionless numbers of the SCVs observed in the VTR during the Ilhas 1 survey. We calculate the bulk Rossby number ($Ro_b = \overline{\mathbf{U}}/(fl)$, where $\overline{\mathbf{U}}$ is the mean value of the velocity magnitude) and the "submesoscale" Burger number ($Bu = (Nh/(fl))^2$, where $h = 150$ m is the SCV thickness) for each SCV and present the results in Table 1. We then compare the results obtained for the VTR SCVs to those presented in the classical work by McWilliams (1985) for SCVs observed and advected by the Gulf Stream: $Ro_b \sim 0.25$ and $Bu = 0.3$. While the Ro_b values found here are close to the former author's estimates, the Bu values are larger. This is probably due to the fact that we are analyzing intrapycnoclinic SCVs (larger N) while McWilliams (1985) examined subpycnoclinic SCVs (smaller N). Nevertheless, the Bu values reflect a more important role for the relative vorticity (in contrast to the stretching vorticity) in our SCVs since they were in a region of stronger stratification. On the other hand, the estimated non-dimensional numbers for the SCVs described in the present work are similar to those described by Riser et al. (1986) and Paillet et al. (2002). The magnitude of these non-dimensional numbers reveals that the vortices present a marginally stable dynamic regime, and therefore relatively distant from the formation region (Buckingham et al., 2021b), where unstable processes are expected (Gula et al., 2019).

We now seek to describe the potential vorticity (PV) structure of the SCVs captured near the CS. We know that the PV of an anticyclonic SCV core is low due to the strong vertical vorticity and weak stratification (Meunier et al., 2018). Low PV values are prone to instabilities (D'Asaro et al., 2011; Thomas et al., 2008, 2013). Here, we evaluate the two-dimensional PV (e.g., Lazaneo et al., 2020; Napolitano et al., 2021; Ramachandran et al., 2018; Thomas et al., 2016) from the objectively mapped field. If one assumes that the features are indeed SCVs and that the sampling of the SCV currents and density occurs through their centers, then an approximation of the Ertel PV is possible.

The Ertel PV is given by

$$q = (f\hat{k} + \nabla \times \mathbf{u}).\nabla b, \tag{2}$$

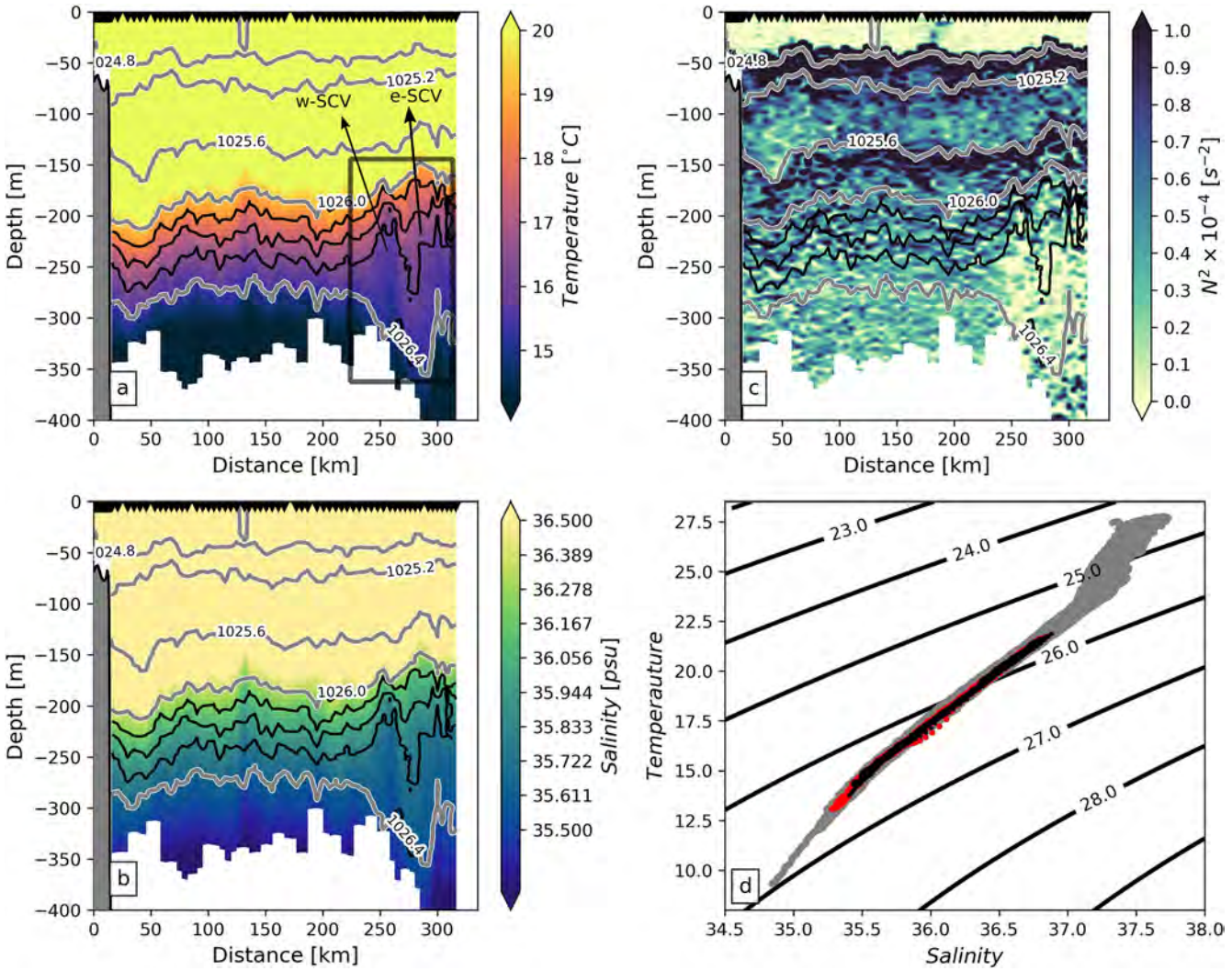

Figure 5. Vertical section of (a) temperature, (b) salinity, and (c) stratification. Gray and black contours represent the isopycnals [kg m^{-3}] along the section. (d) T-S diagram. Gray dots represent points along the whole section, while red and black dots represent T-S pairs within the e-SCV and w-SVC respectively. The origin of the transect starts at the Davis Bank (~20.6°S, 34.7°W). The black rectangle encloses the location of the SCVs.

where $\hat{k}$ is the unit vector, $\mathbf{u} = (u, v, w)$ is the three-dimensional velocity vector, and $b = -g\rho/\rho_0$ is the buoyancy. However, the (in)stability of fluid parcels, in cases where centrifugal accelerations are non-negligible, is governed not by the sign of q but the sign of Lq, where $L = rv + fr^2/2$ is the absolute angular momentum (Buckingham et al., 2021a, 2021b). Here, $r = -12$ km (the negative sign means an anticyclonic vortex) is the radius, which we assume to be the radii of the smaller vortex (w-SCV), to estimate the greatest curvature effect in the flow's PV. Thus, in addition to q under the preceding assumptions and under a gradient wind balance (GWB)

$$q = \underbrace{\left(f + \frac{\partial v}{\partial r} + \frac{v}{r}\right) N^2}_{\text{Barotropic component} - q_{bt}} - \underbrace{\left(f + \frac{2v}{r}\right)\left(\frac{\partial v}{\partial z}\right)^2}_{\text{Baroclinic component} - q_{bc}}, \tag{3}$$

where $N^2 = \partial b/\partial z$ is the stratification, we examine the quantity Lq to verify whether the flow is potentially unstable ($Lq < 0$, (e.g., Buckingham et al., 2021b)). Restricting our solution to regions away from the equator, we can also obtain the nondimensional Ertel PV (q')

$$q' = (1 + Ro_c) - (1 + Cu)Ri^{-1}, \tag{4}$$

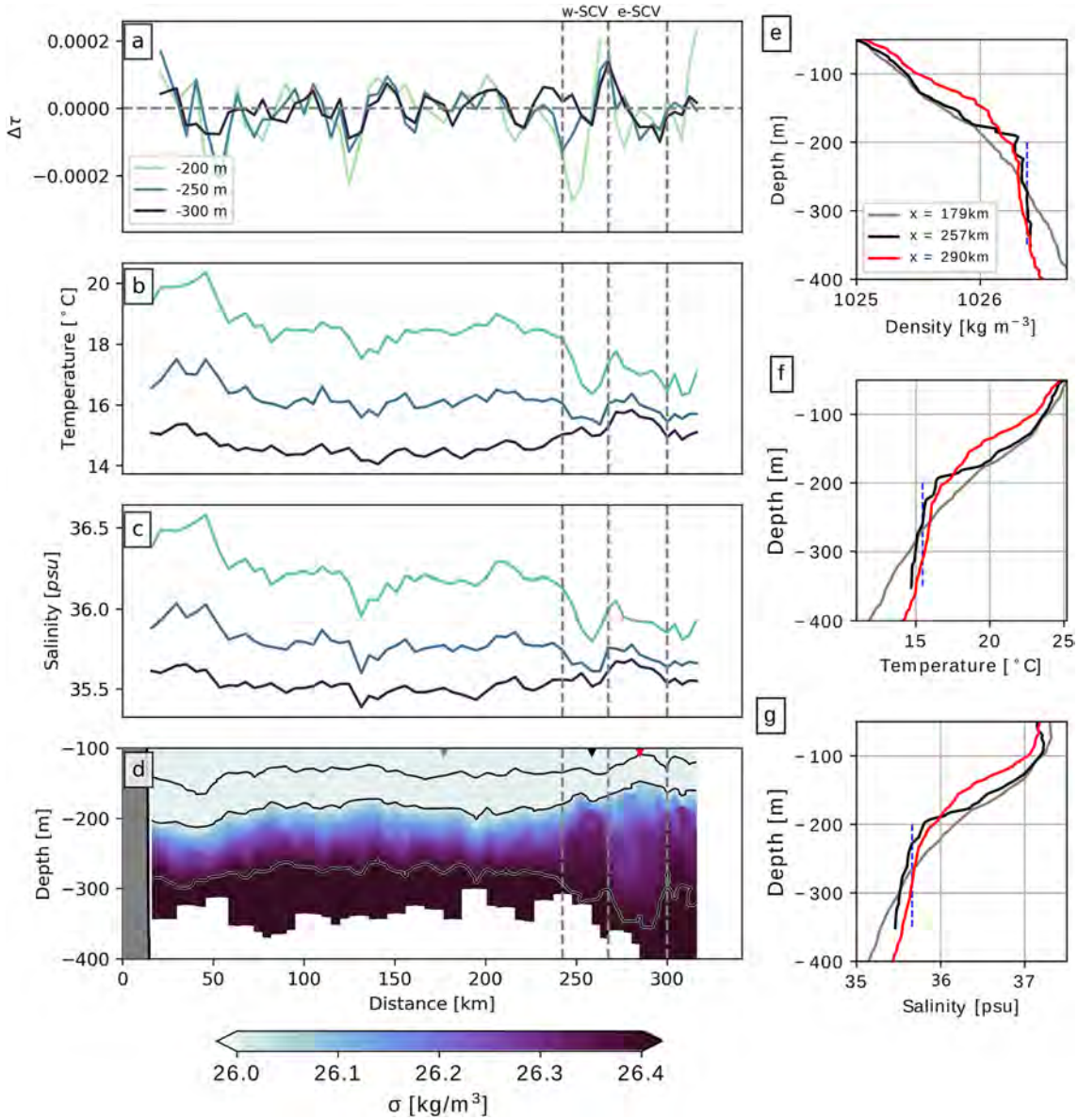

Figure 6. (a) The spiciness, (b) temperature, and (c) salinity variation along-track transect, at z levels. Cyan contours represent $z = -200$ m depth, blue contour represent $z = -250$ m depth, and dark blue represent $z = -300$ m depth. (d) Along-track transect of salinity anomaly S' along isopycnals. The horizontal dashed gray line in (a) represents the 0 of spiciness variation. The horizontal dashed gray lines in (d) represent the upper and lower isopycnal limiting the vertical extension of the e-SCV. The vertical gray dashed lines separate the w-SCV from the e-SCV. The origin of the transect starts at the Davis Bank (~ 20.6°S, 34.7°W). (e) Density, (f) temperature, and (g) salinity profiles in the center of the w-SCV (black) and e-SCV (red) and outside the SCVs (gray). The vertical blue dashed line represents the average value of properties of the profile outside de SCVs. The location of each profile is shown in panel (d) (top triangles).

Table 1
Characterization of the Submesoscale Coherent Vortices (SCVs) in Relation to the Dimensionless Numbers

Number	Symbol	Expression	w-SCV value	e-SCV value
Rossby	Ro_b	$\overline{U}/(fl)$	0.46	0.27
Burger	Bu	$(Nh/(fl))^2$	1.76	0.78

where $Ro_c = \zeta_c/f = (\partial v/\partial r + v/r)f^{-1} = (\partial v/\partial r)f^{-1} + Cu/2$ is the Rossby number for a curved front, $Cu = 2v/rf$ is the curvature number, and $Ri = N^2/(\partial v/\partial z)^2$ is the Richardson number. Thus, the corresponding non-dimensional criterion which accounts for centrifugal accelerations is

$$L'q' = (1 + Cu)(1 + Ro) - (1 + Cu)^2 Ri^{-1} < 0, \quad (5)$$

where $L' = 2\,L/(fr^2) = (1 + Cu)$ is the nondimensional expression of absolute angular momentum (see Buckingham et al., 2021b).

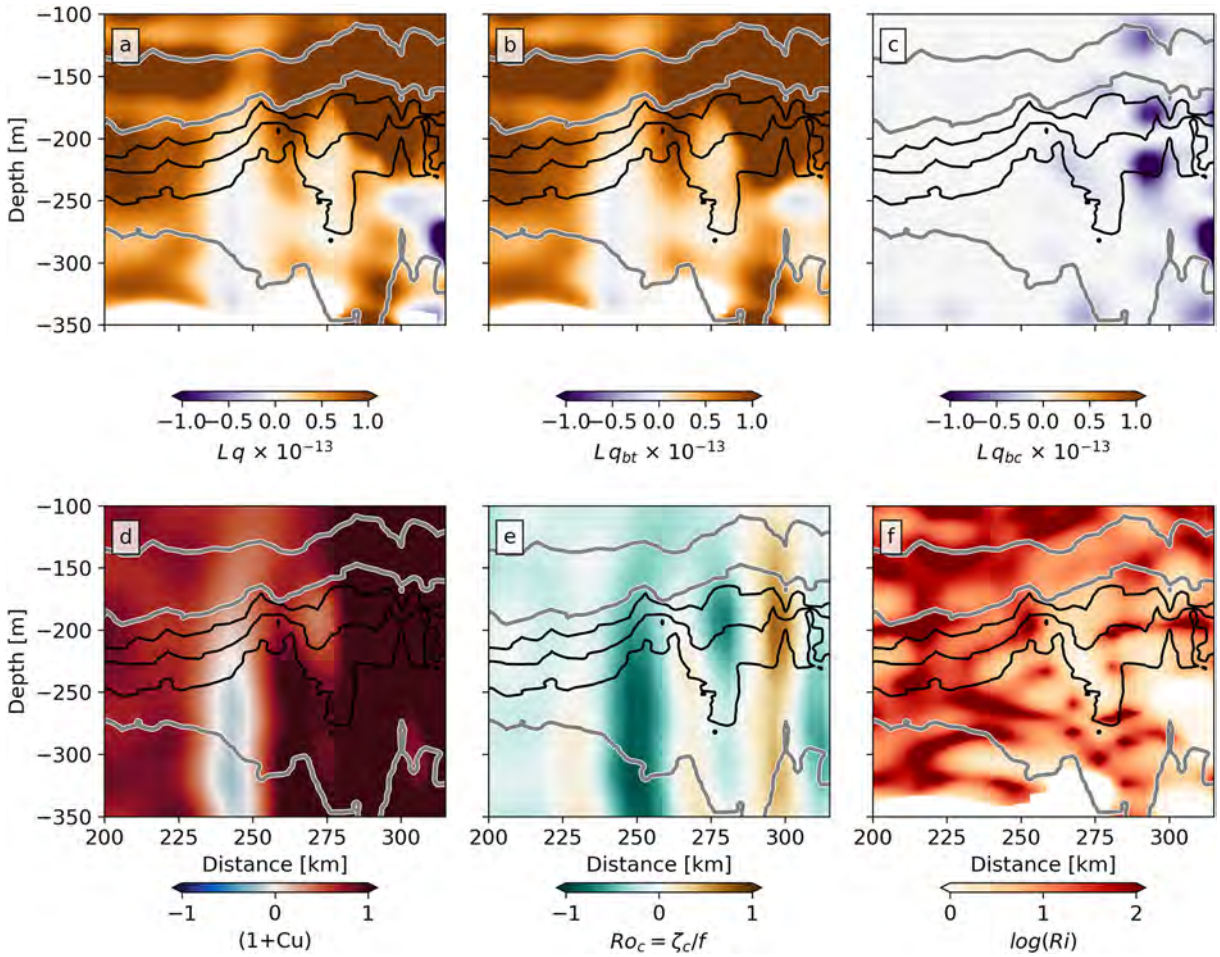

Figure 7. From left to right (top panels) The discriminant Lq, Lq_{bt} (barotropic component), and Lq_{bc} (baroclinic component). From left to right (bottom panels) the discriminant $(1 + Cu)$, where Cu is the curvature of the flow, the Rossby number considering the curvature (Ro_c), and the Richardson number (Ri).

In Figure 7, we show the Ertel PV (from Equation 3) with a greater focus on the two adjacent SCVs. When considering the absolute angular momentum and a flow under GWB, we observe that Lq can be negative inside the SCVs. The low values of Lq (<0 or ~0) are mainly driven by the barotropic component of the potential vorticity (q_{bt}) due to the intense anticyclonic relative vorticity, which in turn is a function of the curvature (Cu) of the flow. In addition to the dominance of the barotropic component of the potential vorticity, the low stratification inside the SCVs and the higher intensity of vertical shear squared (Figure 8a) also suggest a potentially unstable flow driven by the baroclinic part (q_{bc}, $Ri \sim 1$). To categorize the instabilities within the SCV flows, we followed the criteria from Buckingham et al. (2021b), which includes the conservation of absolute angular momentum. We observed that, despite $Lq < 0$, the flow is predominantly stable at the location of the observed SCVs, but with the occurrence of hybrid symmetric/centrifugal instability (Figure 8b). Although these results suggest the occurrence of instabilities, they only occur in small extensions of the vortices. This may be due to (a) the sampling strategy, that is, the horizontal resolution of the data set may not be enough to capture and categorize the instabilities, (b) due to the smoothing of the data (temperature, salinity, and velocity) by the calculation of the objective field to reduce the differences in the sampling scales, or due to (c) the interaction of the adjacent SCVs, which can mask, or even stabilize, the flow. It is noteworthy that in the present work, we do not analyze the effect of the interaction of the vortices, but we described their occurrence in the VTR region. The results suggest that SCVs are prone to centrifugal and symmetrical instabilities, which ultimately implies that instabilities may draw energy from the flow.

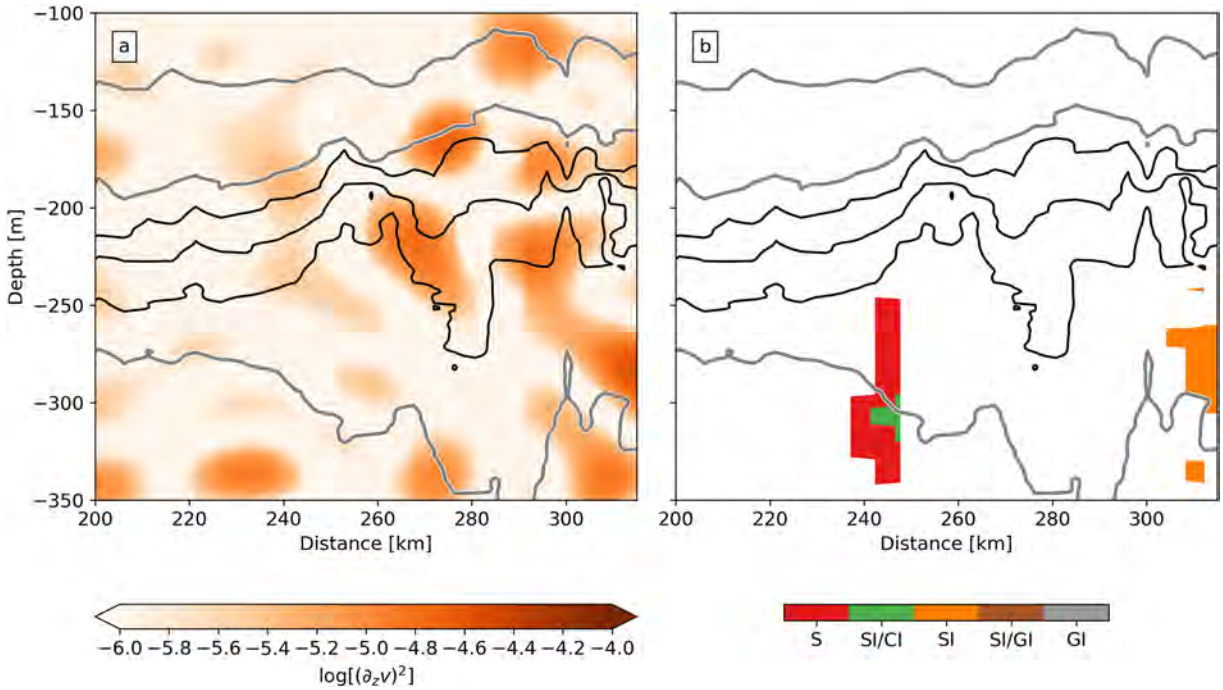

Figure 8. (a) Vertical section of the vertical shear squared in logarithmic scale. (b) The panel shows the location of different type of instabilities for anticyclonic flow ($Ro_c < 0$). S: stable ($\phi_0 < \phi_1 < 0$, see Buckingham et al., 2021b). SI: symmetric instability, CI: centrifugal instability and GI: gravitational instability. Where $\phi_0 = \tan^{-1}[-(1 + Cu)\,(1 + Ro_c)]$, and $\phi_1 = \tan^{-1}[-(1 + Cu)^2 Ri^{-1}]$. Gray contours represent isopycnals highlitening the upper and bottom of the submesoscale coherent vortices (SCVs), and black contourd represent the isopycnal crossing the SCVs.

4. Pathway for Energy Dissipation

One of the defining characteristics of anticyclonic SCVs is that they exhibit anomalously low PV (e.g., Gula et al., 2019), as do those observed during the Ilhas 1 survey. The origin of this unstable, or marginally stable regime in their cores comes from their site of origin. PV reduction can occur from convective and frontal processes at the surface (Thomas, 2005; Thomas et al., 2013) and subsurface frictional forces due to flow separation near topography (D'Asaro, 1988; Gula et al., 2019). In both cases, the manifestation of instabilities in this dynamical regime involves smaller-scale turbulence that cascades energy down to dissipation (McWilliams, 2016). Our in-situ, microstructure measurements reveal that the dissipation rate ε of turbulent kinetic energy (TKE) within the SCVs is two orders of magnitude larger than in surrounding waters (Figures 9a–9f), thus showing that SCVs are important agents for energy dissipation.

From the integration of the spectrum of velocity fluctuations (Φ), assuming isotropic turbulence, we estimated the TKE dissipation rates (ε) for segments of the water column,

$$\varepsilon = \frac{15}{2}\nu\overline{\left(\frac{\partial u'}{\partial z}\right)^2} = \frac{15}{2}\nu\int_1^{k_{\max}} \Phi(k)dk \ \ [\mathrm{W\ kg^{-1}}], \tag{6}$$

where ν is the kinematic molecular viscosity, $\partial u'/\partial z$ can be any of the six components of the shear fluctuations, and $k_{\max}$ is the maximum wavenumber determined by the fast Fourier transform with a 50% overlap for each vertical segment. For this study, we chose segments of the water column corresponding to 1 s to convert temporal derivatives to spatial derivatives, assuming a frozen field hypothesis (Taylor, 1938). Lazaneo et al. (2020) showed that there is no significant ε variation from the different lengths of segments. Since the VTR presents very abrupt changes of depth, using a bin size of 1 s to estimate ε provides a reasonable number of values, mainly over shallow regions. The shorter the segment length, the greater the noise of the estimation. However, using an average from multiple microstructure profilers deployed at the same station, we can reduce the noise while keeping the strongest signal (e.g., Doubell et al., 2018; Lazaneo et al., 2020). Comparing the measured spectrum with the theoretical Nasmyth spectrum (Figure 9g), we assure better reliability. The composite mean of the TKE dissipation

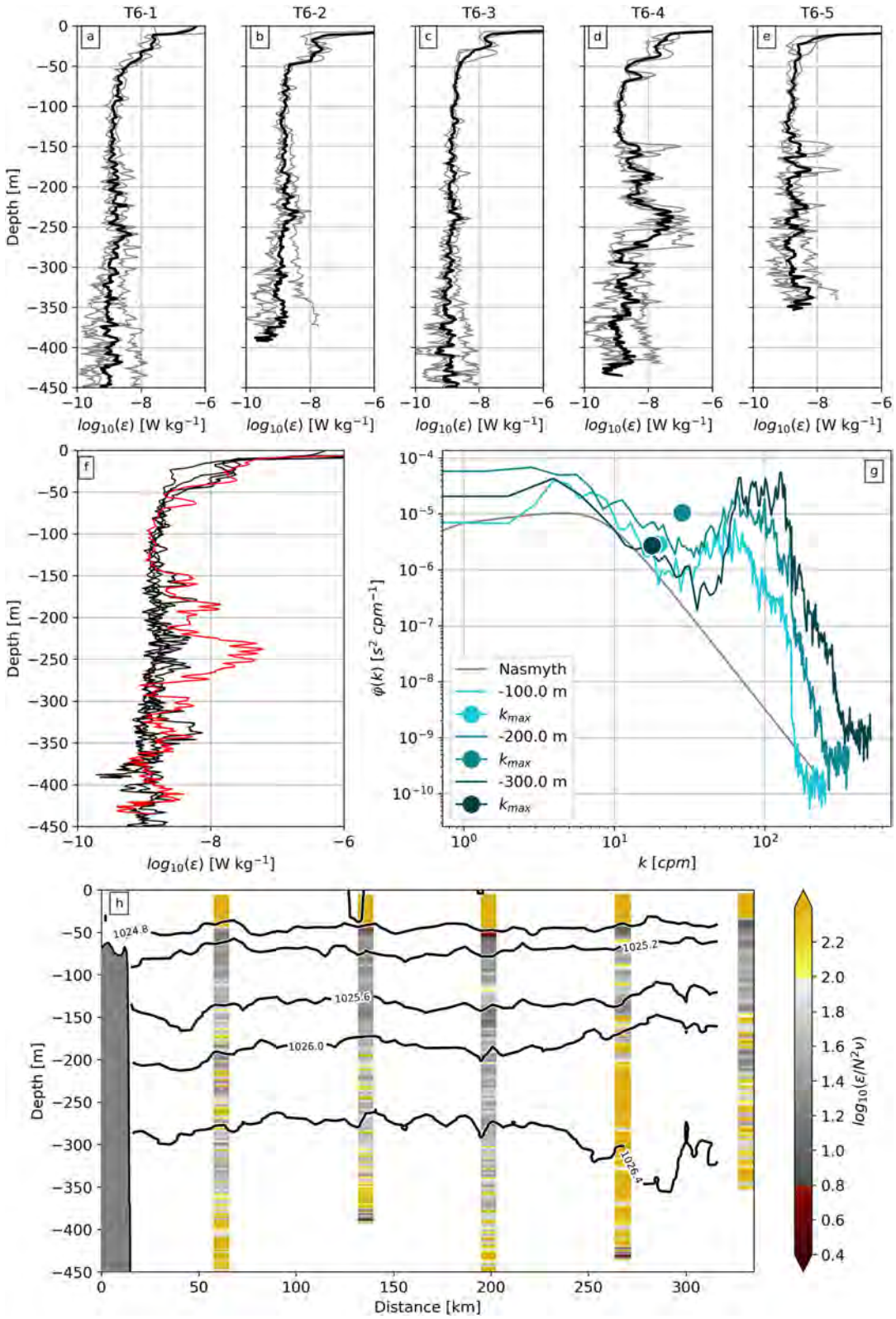

Figure 9. (a–e) Vertical profiles of TKE dissipation rates. Gray lines represent n-cast deployed at each oceanographic station, while black lines show the average profile at each station. Panel f shows the average profiles presented in top panels together, highlighting the amount of energy dissipation rates within the SCV at station T6-4 (red). (g) Shear spectrum observed by a VMP at different depths at station T6-4 superimposed on the Nasmyth spectrum (gray curve), where k_{max} is the integration cutoff wavenumber. (h) Spatial distribution of the buoyancy Reynolds number ($Re_b = \varepsilon/\nu N^2$) superimposed on the isopycnal surfaces (black contours).

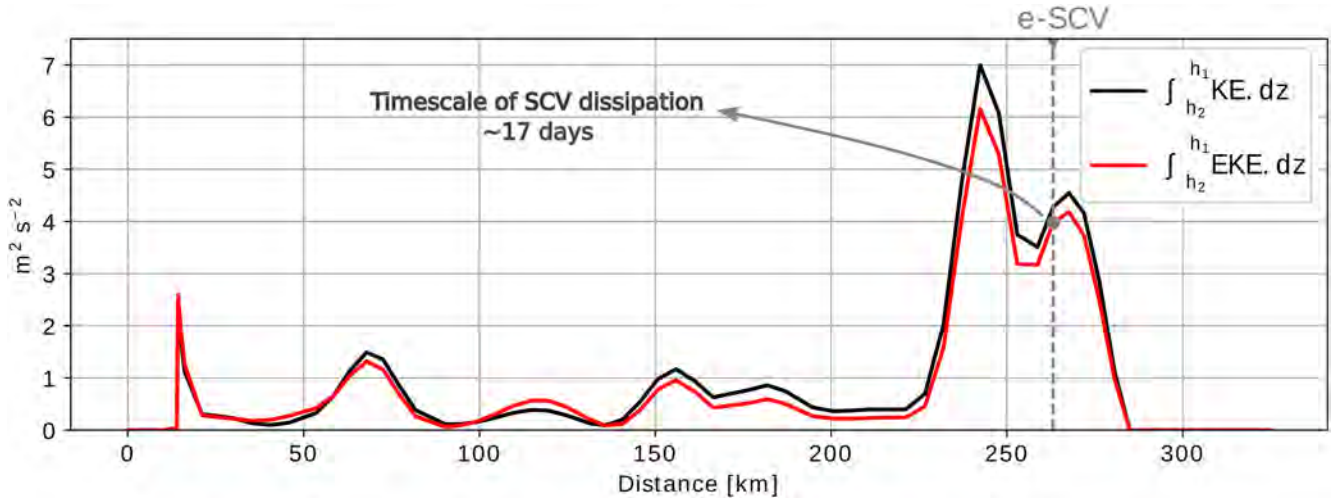

Figure 10. Spatial variation of the kinetic energy (KE, black) and the eddy kinetic energy (EKE, red) vertically integrated into the water column (between $h_1 = -300$ and $h_2 = -200$ m). The vertical dashed gray line depicts the location of the microstructure profiler, which captured the submesoscale coherent vortex (SCV). The gray dot represents the amount of EKE used to estimate the timescale of the SCV dissipation.

rate shows a nearly constant amount of energy dissipation along the water column (Figure 9). However, the last two stations nearby the CS show a significant increase in the amount of energy dissipation at the sub-thermocline level. From 150 m depth to 300 m depth at station T6-4, a great burst of energy dissipation reaches values typical of the mixed layer. The turbulence activity parameter ($\varepsilon/\nu N^2$), also called buoyancy Reynolds number (Re_b), provides an additional indication of the degree of turbulence in the SCV core. This parameter scales with turbulent diffusivity from the Osborn model (Osborn, 1980) for the intermediate regime. On the other hand, the diffusivity scales with $(Re_b)^{1/2}$ for the energetic regime, corresponding to higher values of Re_b and growing turbulence (Shih et al., 2005). For the e-SCV, Re_b is extremely high, in fact comparable to the turbulent regime of the mixed layer (Figure 9h).

We show that the SCVs can develop barotropic (centrifugal instability) and baroclinic (symmetric instability) instabilities, resulting in energy transfer toward dissipative scales (forward energy cascade). Furthermore, we confirm the occurrence of dissipative and diffusive processes by measuring the vertical shear variance inside and outside the vortices. Thus, we conclude that (a) the effect of the curvature of the flow, (b) the intense horizontal shear (large Ro_c), and (c) the combined effects of large vertical shear and low stratification (small Ri), are plausible sources for the high EKE ($(u'^2 + v'^2)/2$) of the features. In Figure 10, we show that the vertically integrated EKE contained inside the SCVs can be 10 times higher than outside of the SCVs. Comparing the integral EKE within the SCV with the integral of the TKE dissipation rates at the same depth interval ($h_1 = -200$ and $h_2 = -300$ m)

$$\frac{\int_{h_2}^{h_1} EKE\,\mathrm{d}z}{\int_{h_2}^{h_1} \epsilon\,\mathrm{d}z}\,\frac{[\mathrm{m^3\,s^{-2}}]}{[\mathrm{m^3\,s^{-3}}]} = \text{timescale}\,[\mathrm{s}], \tag{7}$$

we obtain that the lower bound vortex dissipation timescale is approximately 17 days. It should be noted that we only consider the EKE available at the sampling time and a constant dissipation rate. Therefore, we only compute the energy to be dissipated (assuming that the EKE sources cease) and not that which may have already been dissipated since the beginning of the SCV life cycle. The redistribution of energy across the eddy-mean reservoirs may occur throughout the whole vortex lifetime. As part of the energy is dissipated by turbulent processes, barotropic and baroclinic instabilities, via horizontal shear production and buoyancy flux, respectively (e.g., Gula et al., 2016), may feedback into the EKE reservoir, and hence the difference in the dissipation timescale obtained and the SCVs lifetime (e.g., McDowell & Rossby, 1978; McWilliams, 1985). The complete dissipation of such vortices occurs by fusion into the larger eddies or by erosion due to interactions with topography (Morvan et al., 2019). Considering the high population of the undersampled SCVs in the interior of the oceans (McCoy et al., 2020), we suggest that the SCVs are one of the keys to understanding the interior ocean's energy budget, not limiting the occurrence of dissipative processes attributed only to boundary layers. Further studies are needed to

clarify the eddy-mean energy conversion mechanisms throughout the SCVs lifetime and their role in the oceanic energy budget.

The distance between consecutive microstructure profilers along the transect does not permit the estimation of the TKE dissipation of both SCVs. However, the combination of weak stratification, high vorticity, low PV, and low *Ri* corroborates the hypothesis of intense mixing and energy dissipation within such features. On the one hand, part of the measured energy dissipation could arise from the manifestation of internal waves generated in the VTR (Paiva et al., 2018) by the acceleration of the flow or by the collapse of fronts (Shakespeare & Taylor, 2014) or due to the interaction with the local topography. Inertial oscillations are excited in boundary layers (Barkan et al., 2017; Nikurashin & Ferrari, 2011; Thomas, 2017), radiated, and reabsorbed by larger-scale flows, while only a small fraction of the energy of these oscillations is dissipated (Nagai et al., 2015). On the other hand, the correspondence of negative, or even low PV within the SCVs, is associated with the large TKE dissipation rates (e.g., Nagai et al., 2021). Finally, the evidence of the anomalous amount of energy dissipation in the e-SCV core evinces the role of SCVs in the ocean energy budget. Nevertheless, it remains an open question where these vortices have been generated, and another unsettled issue is whether or not the VTR is prone to form such small features. To address these questions, we inspect the mesoscale circulation pattern using altimetry data and compare this scenario with the previous findings from the Ilhas 1 survey.

5. Mesoscale Circulation Pattern Along the VTR

In this section, we address the possibility that the SCVs captured by the Ilhas 1 survey sampling had been formed through interaction of an ocean current with the VTR. Mesoscale eddies contain the majority of the kinetic energy of ocean currents. The term "eddies" is used here to represent the various forms of ocean current variability at the mesoscale: vortices, rings, and current meanders (e.g., Fu, 2006). The VTR is located in the northwestern limb of the South Atlantic subtropical gyre circulation (Stramma & England, 1999). The region is potentially along the path of the southern branch of the SEC (Garzoli & Matano, 2011; Nencioli et al., 2018). Sea surface height measurements made by microwave altimeters can be used to obtain a synoptic view of mesoscale eddies (Chelton et al., 2011; Fu et al., 2010). From the altimetry data, it is possible to map the pathways of the mesoscale eddies reaching the VTR along with the SEC.

The surface circulation pattern through the period of the austral summer via altimetry data shows a mesoscale anticyclonic signal over the CS (Figure 2). From the daily output of the absolute dynamic topography, we tracked this signal backward in time to investigate its pathway prior to reaching the sampled area (Figure 11). In early November 2016, the anticyclonic meander was observed southeast of Trindade Island, centered at 22°S 27.5°W (Figures 11a and 11e). We defined the eddy as a region with values of Okubo-Weiss parameter $W < -0.2\sigma_W$, where σ_W is the spatial standard deviation of W. This definition is shown to be appropriate to detect mesoscale eddies from sea level anomaly (e.g., Isern-Fontanet et al., 2006; Zhang et al., 2016). In December, the northern edge of the anticyclone obliquely hits the island, deforming itself and enhancing its absolute dynamic topography (Figures 11b and 11f). After the interaction with the island, the geostrophic vorticity of the anticyclone decayed, keeping its core south of the island. In mid-January, this anticyclonic signal appears as a westward-propagating meander reaching the CS (Figures 11d and 11h). While the surface mesoscale circulation pattern depicted from the altimeters shows the anticyclone passing across the CS, the ADCP measurements show this eddy signal at the surface, with the maximum subsurface velocity related to the SCVs embedded in its flow (Figure 2).

As a mesoscale flow passes by a topographic obstacle, submesoscale relative vorticity grows downstream (Gula et al., 2016). The combination of intense relative vorticity and low stratification may lead to centrifugal instabilities at the island wakes (e.g., Srinivasan et al., 2019). The bottom boundary condition imposed by the physical barrier of topography triggers the intense horizontal shear in a low-stratified environment below the pycnocline. Under certain conditions, these unstable wakes evolve to form SCVs (Srinivasan et al., 2019) without a surface signature (Gula et al., 2019). The tendency toward instabilities in the anticyclonic SCV cores (low PV values) may come from their generation sites. The impermeability theorem states that PV is conserved across two isopycnal surfaces (Haynes & McIntyre, 1987). Thus, the PV reduction should occur through diabatic processes or frictional forces within the two bounded isopycnals (Thomas, 2005), leading to negative PV anomalies within the SCV cores (see Gula et al., 2019). Despite the low, but positive values of PV, mainly driven by the high horizontal

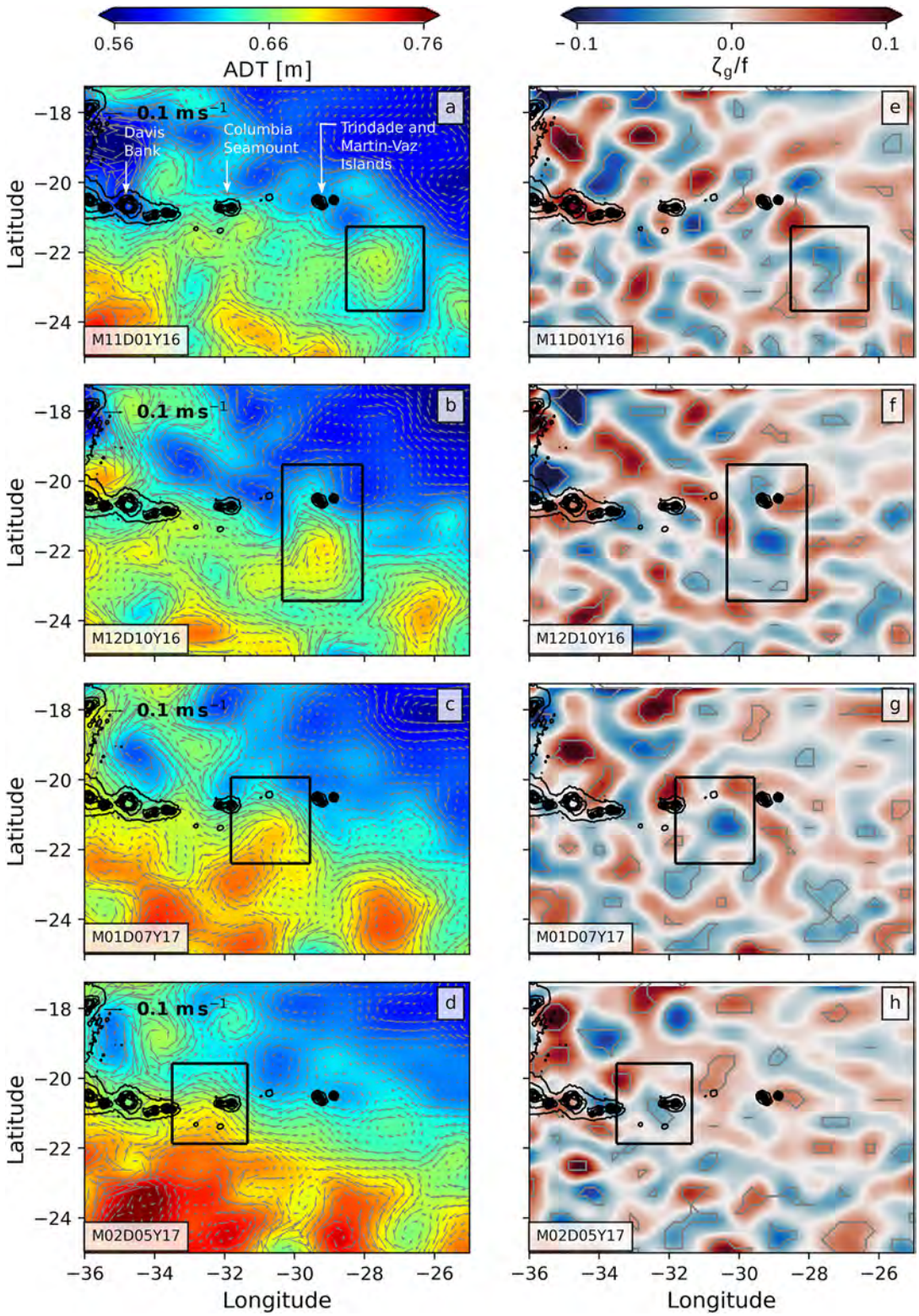

Figure 11. (a–d) Daily snapshots of the absolute dynamic topography (background color) with its respective velocity field (gray arrows) (e–h) Daily snapshots of ζ_g/f (background color), where $\zeta_g = \partial v_g/\partial x - \partial u_g/\partial y$. u_g and v_g are the geostrophic velocity components derived from CMEMS. Gray contours represent the Okubo-Weiss parameter for eddy detection. Black contours represent the isobaths around the VTR. The area used to calculate the standard deviation is the area shown on the maps.

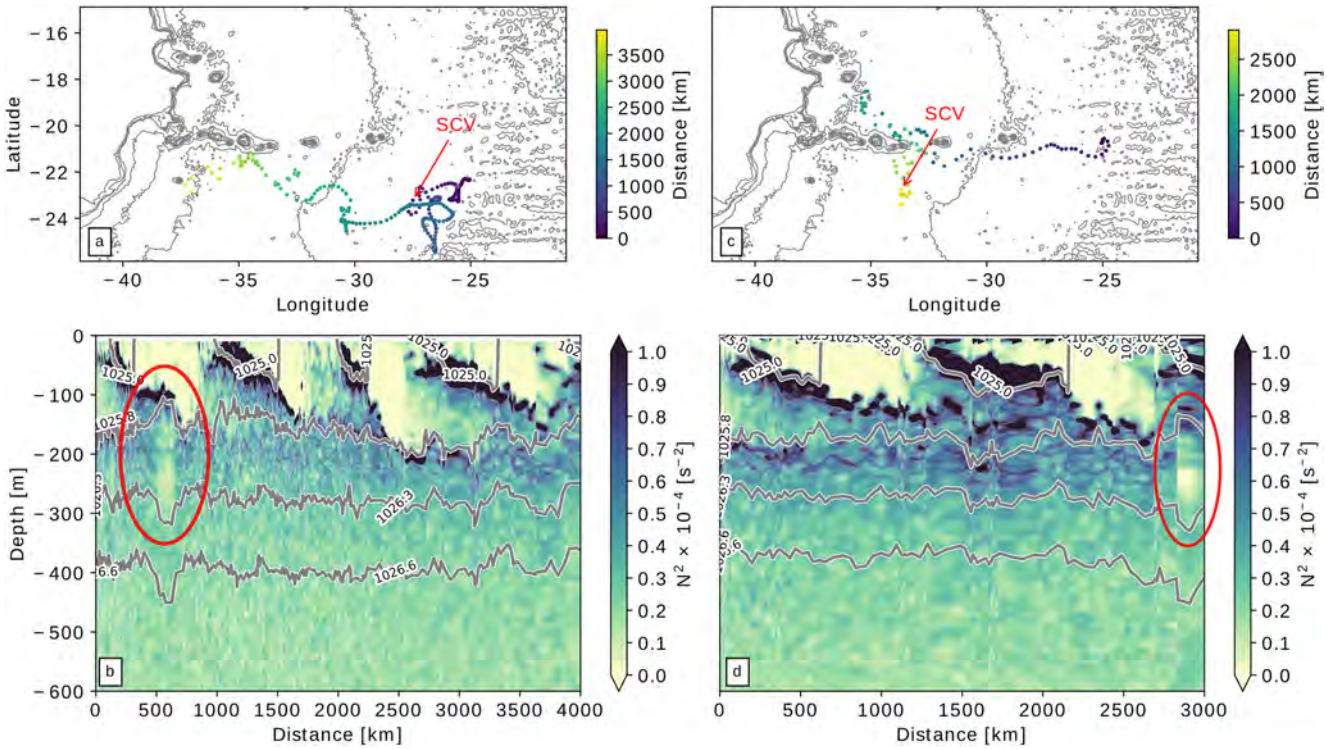

Figure 12. Trajectories of the Argo floats (a) 3901496, and (c) 3902125 based on the distance from their origin. Vertical section of the stratification from Argo floats (b) 3901496, and (d) 3902125. The red arrows represent the location of the submesoscale coherent vortex in each Argo float trajectory (Data source: http://www.coriolis.eu.org/).

shear, the weak stratification can be sporadically overcome by the vertical shear, leading to small-scale turbulence and mixing.

Long-lived SCVs may also reach the VTR region from remote locations. Analysis of Argo float data has revealed that SCVs are ubiquitous in the ocean, and thus of great importance in the large-scale transport of tracers (McCoy et al., 2020). The authors argued that tracked SCVs are, in part, generated in eastern boundary upwelling systems, in marginal sea overflows– influenced by capes and promontories– along open ocean fronts, and ultimately travel across the ocean basins. To provide context to the present work, we therefore depict the trajectory and measurements of two Argo floats that captured SCV-like structures in their pathways (Figure 10). The first Argo float trajectory shows the presence of one SCV away from the VTR (Figures 12a and 12c). The westward flow of the SEC can advect the SCV-like structure along the South Atlantic basin since the β effect has a relatively minor influence on its trajectory (Dewar & Meng, 1995). On the other hand, the trajectory of a second Argo float shows the occurrence of one SCV to the south of the VTR (Figures 12b and 12d). We cannot determine whether or not the latter SCV, captured by the Argo float, was generated at the VTR. Therefore, SCV-like structures can not only reach the VTR region by the SEC advection, but can also be locally generated.

Observations of these small structures in the ocean, such as the SCV captured during the Ilhas 1 survey, are challenging due to the vortices' small size and the portion of the water column they occupy (below the mixed layer). Nevertheless, we see them as keys to understanding the ocean interior variability since they transport water mass from their site of origin (life cycle on the order of years; McWilliams, 1985, 2016) and lead to energy dissipation enhancement through centrifugal instabilities (Srinivasan et al., 2019). Most of these findings gathered from the literature evinced the importance of submesoscale features to the ocean energy budget. However, these studies employed numerical simulations and computed the energy budget from the outputs. The present study is observational, and neither the energy budget nor the SCV site of origin estimate can be determined from our data. Despite that, we see as likely that the captured SCVs near the CS are a result of the interaction of the meandering SEC with the VTR.

6. Summary and Concluding Remarks

In this study, we describe unprecedented observations of two adjacent SCVs embedded in the SEC as it flowed across the VTR. These intrapycnoclinic features occupied the density range of 1,026 and 1026.4 kg/m^3, and revealed a vertical extension of approximately 150 m. The radii of the two submesoscale vortices were 12 and 16 km, and were characterized by bulk Rossby numbers of 0.46 and 0.27, and Burger numbers of 1.76 and 0.78, respectively. The SCVs were characterized by homogenized SACW waters bounded by two convex-lens-shaped isopycnals and intense relative vorticity. The combination of temperature, salinity, and velocity measurements allowed us to determine the marginally stable dynamic regime inside the SCVs, which ultimately suggests small-scale turbulence cascading energy down to dissipation via centrifugal and symmetric instabilities. Our in situ microstructure observations revealed that the e-SCV contained dissipation rates at least two orders of magnitude higher than the surrounding waters, comparable to turbulence of the mixed layer. This anomalous energy dissipation rate confirms the occurrence of turbulence inside the e-SCV.

The limited spatial distribution of sampling data does not permit the determination of the place of formation of the captured SCVs. Temperature and salinity signatures within each SCV exhibit homogenized SACW in their cores, with tiny deviations relative to the surrounding waters. These results suggest a remote site for the SCVs' generation, but not necessarily out of the VTR region, since flow-topography interaction is one of the principal candidates for SCV generation. We provide evidence of the flow-topography interaction by tracking an SEC meander passing by the Trindade Island 2 months earlier than the period of the Ilhas 1 survey (austral summer). This mesoscale anticyclonic meander was observed over the CS through altimetry and ADCP measurements during our oceanographic survey. The pathway of such a mesoscale anticyclone indicates its crossing of the Trindade Island 2 months earlier. The archipelago of Trindade and Martin-Vaz is the easternmost isolated set of islands along the SEC pathway in the western South Atlantic basin. Such interaction could result in SCV generation through centrifugal instability in the island wakes (D'Asaro, 1988). Submesoscale-resolving simulations are already under development to verify if the interaction of the eddy-rich SEC with the VTR is indeed prone to the generation of SCVs. However, the lack of observations in the region is still the main constraint to better understanding SCVs and their roles in regional ocean circulation.

Moreover, since SCVs have been observed throughout the world's oceans, they may make a significant contribution to the energy budget of the oceans. The research presented here therefore encourages further research into better understanding the role of SCVs in (global) ocean circulation, including their impacts on tracer and energy fluxes.

Acknowledgments
The authors would like to thank Jonathan Gula and Christian Buckingham for their careful and insightful comments which substantially improved the initial manuscript. The authors also would like to thank Frank O. Smith for copy editing and proofreading this manuscript and Dante C. Napolitano for the help in the ADCP data processing. This study is part of the "Projeto Ilhas"(Processo CNPq 458583/2013-8). C. Z. Lazaneo acknowledges support from Coordenação de Aperfeiçoamento de Pessoal de Nível Superior - Brasil (CAPES) - Finance Code 001, and from Conselho Nacional de Desenvolvimento Científico e Tecnológico - CNPq (Processo 205857/2018–3). P. H. R. Calil acknowledges support from Projeto ILHAS (Processo CNPq 458583/2013-8). A. Tandon acknowledges support from NSF Grant OCE1755313 and ONR N000141812799. I. C. A. da Silveira acknowledges support from CNPq (Grant 307814/2017-3), Projeto SUBMESO (Processo CNPq 442926/2015-4), Projeto REMARSUL (Processo CAPES 88882.158621/2014-01), and Projeto VT-Dyn (Processo FAPESP 2015/21729-4). The authors are very grateful to the crew of R/V Alpha Crucis and, in particular, Captain José H. M. Rezende.

Data Availability Statement

The data were provided by the Copernicus Marine and Environment Monitoring Service (CMEMS, http://marine.copernicus.eu) and from the Argo program, distributed by Coriolis Operational Oceanography (http://www.coriolis.eu.org/). The data used in this study can be obtained at https://jmp.sh/5zPZzCC.

References

Alberoni, A. A. L., Jeck, I. K., Silva, C. G., & Torres, L. C. (2020). The new digital terrain model (DTM) of the Brazilian continental margin: Detailed morphology and revised undersea feature names. *Geo-Marine Letters*, *40*(6), 949–964. https://doi.org/10.1007/s00367-019-00606-x

Assassi, C., Morel, Y., Vandermeirsch, F., Chaigneau, A., Pegliasco, C., Morrow, R., et al. (2016). An index to distinguish surface- and subsurface-intensified vortices from surface observations. *Journal of Physical Oceanography*, *46*(8), 2529–2552. https://doi.org/10.1175/JPO-D-15-0122.1

Bane, J. M., O'Keefe, L. M., & Watts, D. R. (1989). Mesoscale eddies and submesoscale, coherent vortices: Their existence near and interactions with the Gulf Stream. *Elsevier Oceanography Series*, *50*, 501–518. https://doi.org/10.1016/S0422-9894(08)70204-6

Barkan, R., Winters, K. B., & Mcwilliams, J. C. (2017). Stimulated imbalance and the enhancement of eddy kinetic energy dissipation by internal waves. *Journal of Physical Oceanography*, *47*(1), 181–198. https://doi.org/10.1175/JPO-D-16-0117.1

Buckingham, C. E., Gula, J., & Carton, X. (2021a). The role of curvature in modifying frontal instabilities. Part II: Application of the criterion to curved density fronts at low Richardson numbers. *Journal of Physical Oceanography*, *51*(2), 317–341. https://doi.org/10.1175/jpo-d-20-0258.110.1175/jpo-d-20-0258.1

Buckingham, C. E., Gula, J., & Carton, X. (2021b). The role of curvature in modifying frontal instabilities. Part I: Review of theory and presentation of a nondimensional instability criterion. *Journal of Physical Oceanography*, *51*(2), 299–315. https://doi.org/10.1175/jpo-d-19-0265.1

Charney, J. G. (1971). Geostrophic turbulence. *Journal of the Atmospheric Sciences*, *28*(6), 1087–1095. https://doi.org/10.1175/1520-0469(1971)028<1087:gt>2.0.co;2

Chelton, D. B., Schlax, M. G., & Samelson, R. M. (2011). Global observations of nonlinear mesoscale eddies. *Progress in Oceanography*, *91*(2), 167–216. https://doi.org/10.1016/j.pocean.2011.01.002

D'Asaro, E. A. (1988). Generation of submesoscale vortices: A new mechanism. *Journal of Geophysical Research*, *93*(C6), 6685. https://doi.org/10.1029/jc093ic06p06685

D'Asaro, E., Lee, C., Rainville, L., Harcourt, R., & Thomas, L. (2011). Enhanced turbulence and energy dissipation at ocean fronts. *Science*, *332*(6027), 318–322. https://doi.org/10.1126/science.1201515

de Marez, C., Carton, X., Corréard, S., L'Hégaret, P., & Morvan, M. (2020). Observations of a deep submesoscale cyclonic vortex in the Arabian Sea. *Geophysical Research Letters*, *47*(13). https://doi.org/10.1029/2020GL087881

Dewar, W. K., & Meng, H. (1995). The propagation of submesoscale coherent vortices. *Journal of Physical Oceanography*, *25*(8), 1745–1770. https://doi.org/10.1175/1520-0485(1995)025<1745:tposcv>2.0.co;2

Doubell, M. J., Spencer, D., van Ruth, P. D., Lemckert, C., & Middleton, J. F. (2018). Observations of vertical turbulent nitrate flux during summer in the Great Australian Bight. *Deep-Sea Research Part II: Topical Studies in Oceanography*, *157–158*, 27–35. https://doi.org/10.1016/j.dsr2.2018.08.007

Dugan, J. P., Mied, R. P., Mignerey, P. C., & Schuetz, A. F. (1982). Compact, intrathermocline eddies in the Sargasso Sea. *Journal of Geophysical Research*, *87*(C1), 385. https://doi.org/10.1029/JC087iC01p00385

Ferrari, R., & Rudnick, D. L. (2000). Thermohaline variability in the upper ocean. *Journal of Geophysical Research*, *105*(C7), 16857–16883. https://doi.org/10.1029/2000jc900057

Firing, E. (1995). *Processing ADCP data with the CODAS software system version 3.1*. Joint Institute for Marine and Atmospheric Research, University of Hawaii & National Oceanographic Data Center.

Frenger, I., Bianchi, D., Stührenberg, C., Oschlies, A., Dunne, J., Deutsch, C., et al. (2018). Biogeochemical role of subsurface coherent eddies in the ocean: Tracer cannonballs, hypoxic storms, and microbial stewpots? *Global Biogeochemical Cycles*, *32*(2), 226–249. https://doi.org/10.1002/2017GB005743

Fu, L.-L. (2006). Pathways of eddies in the South Atlantic Ocean revealed from satellite altimeter observations. *Geophysical Research Letters*, *33*(14). https://doi.org/10.1029/2006GL026245

Fu, L.-L., Chelton, D. B., Le Traon, P.-Y., & Morrow, R. (2010). Eddy dynamics from satellite altimetry. *Oceanography*, *23*(4), 14–25. https://doi.org/10.5670/oceanog.2010.02

Garzoli, S. L., & Matano, R. (2011). The South Atlantic and the Atlantic meridional overturning circulation. *Deep-Sea Research Part II: Topical Studies in Oceanography*, *58*(17–18), 1837–1847. https://doi.org/10.1016/j.dsr2.2010.10.063

Gula, J., Blacic, T. M., & Todd, R. E. (2019). Submesoscale coherent vortices in the Gulf Stream. *Geophysical Research Letters*, *46*(5), 2704–2714. https://doi.org/10.1029/2019GL081919

Gula, J., Molemaker, M. J., & McWilliams, J. C. (2016). Topographic generation of submesoscale centrifugal instability and energy dissipation. *Nature Communications*, *7*(1). https://doi.org/10.1038/ncomms12811

Haynes, P. H., & McIntyre, M. E. (1987). On the evolution of vorticity and potential vorticity in the presence of diabatic heating and frictional or other forces. *Journal of the Atmospheric Sciences*, *44*(5), 828–841. https://doi.org/10.1175/1520-0469(1987)044<0828:oteova>2.0.co;2

Houry, S., Dombrowsky, E., de Mey, P., & Minster, J.-F. (1987). Brunt-Väisälä frequency and Rossby radii in the south Atlantic. *Journal of Physical Oceanography*, *17*(10), 1619–1626. https://doi.org/10.1175/1520-0485(1987)017<1619:bvfarr>2.0.co;2

Isern-Fontanet, J., García-Ladona, E., & Font, J. (2006). Vortices of the Mediterranean Sea: An altimetric perspective. *Journal of Physical Oceanography*, *36*(1), 87–103. https://doi.org/10.1175/JPO2826.1

Lazaneo, C. Z., Napolitano, D. C., Silveira, I. C. A., Tandon, A., MacDonald, D. G., Ávila, R. A., & Calil, P. H. R. (2020). On the role of turbulent mixing produced by vertical shear between the Brazil current and the intermediate western boundary current. *Journal of Geophysical Research: Oceans*, *125*(1). https://doi.org/10.1029/2019jc015338

Luko, C. D., Silveira, I. C. A., Simoes-Sousa, I. T., Araujo, J. M., & Tandon, A. (2021). Revisiting the Atlantic South Equatorial current. *Journal of Geophysical Research: Oceans*, *126*(7). https://doi.org/10.1029/2021jc017387

McCoy, D., Bianchi, D., & Stewart, A. L. (2020). Global observations of submesoscale coherent vortices in the ocean. *Progress in Oceanography*, *189*, 102452. https://doi.org/10.1016/j.pocean.2020.102452

McDowell, S. E., & Rossby, H. T. (1978). Mediterranean water: An intense mesoscale eddy off the Bahamas. *Science*, *202*(4372), 1085–1087. https://doi.org/10.1126/science.202.4372.1085

McWilliams, J. C. (1985). Submesoscale, coherent vortices in the ocean. *Reviews of Geophysics*, *23*(2), 165. https://doi.org/10.1029/RG023i002p00165

McWilliams, J. C. (2016). Submesoscale currents in the ocean. *Proceedings of the Royal Society A: Mathematical, Physical and Engineering Sciences*, *472*(2189), 20160117. https://doi.org/10.1098/rspa.2016.0117

Ménesguen, C., Hua, B. L., Carton, X., Klingelhoefer, F., Schnürle, P., & Reichert, C. (2012). Arms winding around a meddy seen in seismic reflection data close to the Morocco coastline. *Geophysical Research Letters*, *39*(5). https://doi.org/10.1029/2011gl050798

Meunier, T., Tenreiro, M., Pallàs-Sanz, E., Ochoa, J., Ruiz-Angulo, A., Portela, E., et al. (2018). Intrathermocline eddies embedded within an anticyclonic vortex ring. *Geophysical Research Letters*, *45*(15), 7624–7633. https://doi.org/10.1029/2018GL077527

Molemaker, M. J., Mcwilliams, J. C., & Dewar, W. K. (2015). Submesoscale instability and generation of mesoscale anticyclones near a separation of the California undercurrent. *Journal of Physical Oceanography*, *45*(3), 613–629. https://doi.org/10.1175/jpo-d-13-0225.1

Morvan, M., L'hégaret, P., Carton, X., Gula, J., Vic, C., de Marez, C., et al. (2019). The life cycle of submesoscale eddies generated by topographic interactions. *Ocean Science*, *15*(6), 1531–1543. https://doi.org/10.5194/os-15-1531-2019

Munk, W. (1981). Internal waves and small-scale processes. *Evolution of physical oceanography*, 264–291.

Nagai, T., Hasegawa, D., Tsutsumi, E., Nakamura, H., Nishina, A., Senjyu, T., et al. (2021). The Kuroshio flowing over seamounts and associated submesoscale flows drive 100-km-wide 100-1000-fold enhancement of turbulence. *Communications Earth & Environment*, *2*(1). https://doi.org/10.1038/s43247-021-00230-7

Nagai, T., Tandon, A., Kunze, E., & Mahadevan, A. (2015). Spontaneous generation of near-inertial waves by the Kuroshio Front. *Journal of Physical Oceanography*, *45*(9), 2381–2406. https://doi.org/10.1175/JPO-D-14-0086.1

Napolitano, D. C., da Silveira, I. C. A., Tandon, A., & Calil, P. H. R. (2021). Submesoscale phenomena due to the Brazil current crossing of the Vitória-Trindade Ridge. *Journal of Geophysical Research: Oceans*, *126*(1). https://doi.org/10.1029/2020JC016731

Nencioli, F., Dall'Olmo, G., & Quartly, G. D. (2018). Agulhas ring transport efficiency from combined satellite altimetry and Argo profiles. *Journal of Geophysical Research: Oceans*, *123*(8), 5874–5888. https://doi.org/10.1029/2018jc013909

Nikurashin, M., & Ferrari, R. (2011). Global energy conversion rate from geostrophic flows into internal lee waves in the deep ocean. *Geophysical Research Letters*, *38*(8), L08610. https://doi.org/10.1029/2011GL046576

Osborn, T. R. (1980). Estimates of the local rate of vertical diffusion from dissipation measurements. *Journal of Physical Oceanography*, *10*(1), 83–89. https://doi.org/10.1175/1520-0485(1980)010<0083:eotlro>2.0.co;2

Paillet, J., Le Cann, B., Carton, X., Morel, Y., & Serpette, A. (2002). Dynamics and evolution of a northern meddy. *Journal of Physical Oceanography*, *32*(1), 552–579. https://doi.org/10.1175/1520-0485(2002)032<0055:daeoan>2.0.co;2

Paiva, A. M., Daher, V. B., Costa, V. S., Camargo, S. S. B., Mill, G. N., Gabioux, M., & Alvarenga, J. B. R. (2018). Internal tide generation at the Vitória-Trindade Ridge, South Atlantic Ocean. *Journal of Geophysical Research: Oceans*, *123*(8), 5150–5159. https://doi.org/10.1029/2017JC013725

Ramachandran, S., Tandon, A., Mackinnon, J., Lucas, A. J., Pinkel, R., Waterhouse, A. F., et al. (2018). Submesoscale processes at shallow salinity fronts in the Bay of Bengal: Observations during the winter monsoon. *Journal of Physical Oceanography*, *48*(3), 479–509. https://doi.org/10.1175/jpo-d-16-0283.1

Riser, S. C., Owens, W. B., Rossby, H. T., & Ebbesmeyer, C. C. (1986). The structure, dynamics, and origin of a small-scale lens of water in the western north Atlantic thermocline. *Journal of Physical Oceanography*, *16*(3), 572–590. https://doi.org/10.1175/1520-0485(1986)016<0572:tsdaoo>2.0.co;2

Shakespeare, C. J., & Taylor, J. R. (2014). The spontaneous generation of inertia-gravity waves during frontogenesis forced by large strain: Theory. *Journal of Fluid Mechanics*, *757*, 817–853. https://doi.org/10.1017/jfm.2014.514

Shih, L. H., Koseff, J. R., Ivey, G. N., & Ferziger, J. H. (2005). Parameterization of turbulent fluxes and scales using homogeneous sheared stably stratified turbulence simulations. *Journal of Fluid Mechanics*, *525*, 193–214. https://doi.org/10.1017/S0022112004002587

Srinivasan, K., McWilliams, J. C., Molemaker, M. J., & Barkan, R. (2019). Submesoscale vortical wakes in the lee of topography. *Journal of Physical Oceanography*, *49*(7), 1949–1971. https://doi.org/10.1175/jpo-d-18-0042.1

Srinivasan, K., McWilliams, J. C., Renault, L., Hristova, H. G., Molemaker, J., & Kessler, W. S. (2017). Topographic and mixed layer submesoscale currents in the near-surface southwestern tropical Pacific. *Journal of Physical Oceanography*, *47*(6), 1221–1242. https://doi.org/10.1175/JPO-D-16-0216.1

Stramma, L., & England, M. (1999). On the water masses and mean circulation of the South Atlantic Ocean. *Journal of Geophysical Research: Oceans*, *104*(C9), 20863–20883. https://doi.org/10.1029/1999jc900139

Taylor, G. I. (1938). The spectrum of turbulence. *Proceedings of the Royal Society of London - Series A: Mathematical and Physical Sciences*, *164*(919), 476–490. https://doi.org/10.1098/rspa.1938.0032

Thomas, L. N. (2005). Destruction of potential vorticity by winds. *Journal of Physical Oceanography*, *35*(12), 2457–2466. https://doi.org/10.1175/JPO2830.1

Thomas, L. N. (2017). On the modifications of near-inertial waves at fronts: Implications for energy transfer across scales. *Ocean Dynamics*, *67*(10), 1335–1350. https://doi.org/10.1007/s10236-017-1088-6

Thomas, L. N., Tandon, A., & Mahadevan, A. (2008). Submesoscale processes and dynamics. *Geophysical Monograph Series*, *177*, 17–38. https://doi.org/10.1029/177GM04

Thomas, L. N., Taylor, J. R., D'Asaro, E. A., Lee, C. M., Klymak, J. M., & Shcherbina, A. (2016). Symmetric instability, inertial oscillations, and turbulence at the Gulf Stream front. *Journal of Physical Oceanography*, *46*(1), 197–217. https://doi.org/10.1175/jpo-d-15-0008.1

Thomas, L. N., Taylor, J. R., Ferrari, R., & Joyce, T. M. (2013). Symmetric instability in the Gulf Stream. *Deep-Sea Research Part II: Topical Studies in Oceanography*, *91*, 96–110. https://doi.org/10.1016/j.dsr2.2013.02.025

Veronis, G. (1972). On properties of seawater defined by temperature. *Deep-Sea Research*, *24*, 325–329.

Vic, C., Gula, J., Roullet, G., & Pradillon, F. (2018). Dispersion of deep-sea hydrothermal vent effluents and larvae by submesoscale and tidal currents. *Deep-Sea Research Part I: Oceanographic Research Papers*, *133*, 1–18. https://doi.org/10.1016/j.dsr.2018.01.001

Vic, C., Roullet, G., Capet, X., Carton, X., Molemaker, M. J., & Gula, J. (2015). Eddy-topography interactions and the fate of the Persian Gulf Outflow. *Journal of Geophysical Research: Oceans*, *120*(10), 6700–6717. https://doi.org/10.1002/2015jc011033

Zhang, Z., Tian, J., Qiu, B., Zhao, W., Chang, P., Wu, D., & Wan, X. (2016). Observed 3D structure, generation, and dissipation of oceanic mesoscale eddies in the South China Sea. *Scientific Reports*, *6*(1), 24349. https://doi.org/10.1038/srep24349